J. Fluid Mech. (1992), *vol.* 245, *pp.* 115–136

A high-order spectral method for nonlinear wave–body interactions

By YUMING LIU, DOUGLAS G. DOMMERMUTH† AND DICK K. P. YUE

Department of Ocean Engineering, Massachusetts Institute of Technology, Cambridge, MA 02139, USA

(Received 17 February 1992)

A high-order spectral method originally developed to simulate nonlinear gravity wave–wave interactions (Dommermuth & Yue 1987*a*), is here extended to study nonlinear interactions between surface waves and a body. The present method accounts for the nonlinear interactions among N_F wave modes on the free surface and N_B source modes on the body surface up to an arbitrary order M in wave steepness. By using fast-transform techniques, the operational count per time step is only linearly proportional to M and N_F (typically $N_F \gg N_B$). Significantly, for a (closed) submerged body, the exponential convergence with respect to M, N_F (for moderately steep waves), and N_B is obtained. To illustrate the usefulness of this method, we apply it to study the diffraction of Stokes waves by a submerged circular cylinder. Computations up to $M = 4$ are performed to obtain the nonlinear steady and harmonic forces on the cylinder and the transmission and reflection coefficients. Comparisons to available measurements as well as existing theoretical/computational predictions are in good agreement. Our most important result is the quantification of the negative horizontal drift force on the cylinder which is fourth order in the incident wave steepness. It is found that the dominant contribution of this force is due to the quadratic interaction of the first- and third-order first-harmonic waves rather than the self-interaction of the second-order second-harmonic waves, which in fact reduces the negative drift force.

1. Introduction

In an earlier work (Dommermuth & Yue 1987*a*, hereinafter denoted DY), a powerful numerical method was developed for modelling nonlinear gravity wave interactions. This method is formally based on the Zakharov equation (Zakharov 1968; Crawford *et al.* 1981)/mode-coupling (Phillips 1960; Benney 1962) idea. The method models interactions up to an arbitrary order M in wave steepness and follows the evolution of a large number (typically $N \sim 10^3$ per dimension) of wave modes through a pseudospectral (Fornberg & Whitham 1978) treatment of the nonlinear free-surface conditions. The method exhibits exponential convergence with M and N for waves up to $\sim 80\%$ ($kA \sim 0.35$) of Stokes limiting steepness (beyond this the convergence is only algebraic), and its efficacy for a variety of wave interaction problems is now well established (see also Dommermuth & Yue 1987*b*).

In this paper, we extend the high-order spectral method to the study of nonlinear wave interactions with a submerged body. The velocity potential at each order $m = 1, \ldots, M$ is considered to result from the combined influence of a dipole distribution

† Present address: SAIC, 10260 Campus Point Drive, San Diego, California, USA.

on the free surface and a source distribution on the body surface. These distributions are in turn expressed as series of spectral modes, in this case Fourier series for closed submerged bodies and periodic (computational) boundary conditions. For N_F and N_B modes respectively on the free surface and body, the convergence of the solution with N_F, N_B and M remains exponentially rapid. This spectral accuracy allows us to obtain high-resolution results for the nonlinear forces on the body and the high-order diffracted wave field.

As a special application, we consider the nonlinear diffraction of Stokes waves by a submerged circular cylinder. This is a well-studied problem for which a number of established theoretical, computational and experimental results are available. Using conformal mapping, Dean (1948) found, to leading order in wave steepness, that a circular cylinder held fixed under waves does not reflect waves, and the transmitted waves merely experience a change in phase but not amplitude. Ursell (1950), using a multipole expansion, found the complete linear solution and showed that it was unique. Following Ursell's approach, Ogilvie (1963) showed that the linear potential leads to a mean (second-order) vertical force but that the horizontal mean force at second order vanishes identically. This last result is in contrast to experimental observations (e.g. Salter, Jeffrey & Taylor 1976) that a free cylinder just awash experiences a negative drift force which causes it to move towards the wavemaker.

Longuet-Higgins (1977) suggested that this negative drift force can be attributed mostly to wave breaking, and, to a lesser degree, to the second-harmonic component of the transmitted wave. The measurements of Miyata *et al.* (1988) and Inoue & Kyozuka (1984) do not support all of Longuet-Higgins' predictions. They found that as the cylinder was moved closer to the free surface, which led to more intense breaking, the negative horizontal drift force was actually reduced and ultimately reversed sign. Using a Stokes expansion, Vada (1987) solved the second-order (frequency-domain) diffraction problem but was unable to calculate all the terms (at fourth order) of the non-vanishing mean horizontal force, since third-order potentials are involved (see §4). For the second-order oscillatory forces, however, Vada's results were in good agreement with the measurements of Chaplin (1984), thereby confirming Chaplin's suggestion that inviscid flow models would be good for Keulegan–Carpenter numbers less than about 2 for second-order forces. As pointed out by Chaplin, however, this is not necessarily true for first-order forces (see §4.3).

A number of fully nonlinear (time-domain) computations of this problem have also been attempted. Vinje & Brevig (1981) used the mixed Eulerian–Lagrangian method of Longuet-Higgins & Cokelet (1976) to study the forces acting on a cylinder under a breaking wave, but their results were only qualitative. Using a similar method, Cointe (1989) obtained higher-order harmonic forces and transmission coefficients but did not focus on the question of the mean horizontal drift force. Stansby & Slaouti (1983) used the method of Zaroodny & Greenberg (1973) to study the forces on cylinders under waves and found that a steady state was rapidly approached. No conclusions were made, however, regarding the steady forces.

For the reflected and transmitted waves, the theoretical prediction of Dean (1948) and Ursell (1950) of no leading-order reflected waves was confirmed by the measurements of Chaplin (1984) to even higher order for mild waves. Grue (1991) performed a careful set of experiments which showed that the transmitted waves are, however, significantly affected by nonlinear wave interactions over the submerged body. Motivated by these results, there are a number of recent theoretical demonstrations (Friis 1990; McIver & McIver 1990; Wu 1991) of the fact that the reflection coefficient is identically zero to second order. The most general result to

date is the work of Palm (1991), who proved that the leading-order component of any harmonic of the reflected wave also vanishes. These analytical results and experimental observations are confirmed by our numerical computations of the high-order (up to $M = 3$) reflected and transmitted waves in §4.

In §2, the mathematical formulation of the high-order spectral method for wave–body interactions is given. The implementation of the numerical method is described in §3. Sources of numerical errors are discussed, and extensive convergence tests are also presented there. In §4, numerical computations for the nonlinear diffraction of a submerged circular cylinder are presented and compared to available measurements and theoretical predictions. Results are given for the nonlinear mean and harmonic amplitudes of the diffracted waves and oscillatory forces, with a special emphasis on the horizontal drift force on the cylinder.

2. Mathematical formulation

We consider the diffraction of nonlinear gravity waves by a fixed, submerged body in deep water. (Without loss of generality, and in anticipation of later application, we assume the body to be a circular cylinder.) A global Cartesian coordinate system (x, y) is located at the mean water level directly above the cylinder centre with y positive upward and x positive in the direction of wave propagation. A local cylindrical coordinate system (r, θ) is placed at the centre of the cylinder, which is at a depth H below the mean water level. Thus, $r^2 = x^2 + (y+H)^2$ and θ is measured counterclockwise from positive x. We assume that the flow is irrotational, and that the fluid itself is homogeneous, incompressible, and inviscid.

The flow is described by a velocity potential $\Phi(x, y, t)$ which satisfies Laplace's equation within the fluid, and vanishes at deep water, $\nabla\Phi \to 0$ as $y \to -\infty$. Following Zakharov (1968), we define the surface potential

$$\Phi^{\mathrm{S}}(x, t) = \Phi(x, \eta(x, t), t), \tag{1}$$

where $y = \eta(x, t)$ denotes the free surface, which we assume to be continuous and single-valued. In terms of Φ^{S}, the kinematic and dynamic boundary conditions on the free surface are respectively

$$\eta_t + \Phi^{\mathrm{S}}_x \eta_x - (1+\eta_x^2)\,\Phi_y(x, \eta, t) = 0, \tag{2a}$$

and

$$\Phi^{\mathrm{S}}_t + g\eta + \tfrac{1}{2}(\Phi^{\mathrm{S}}_x)^2 - \tfrac{1}{2}(1+\eta_x^2)\,\phi_y^2(x, \eta, t) = 0 \tag{2b}$$

for zero atmospheric pressure, where g is the gravitational acceleration. On the cylinder boundary, a no-flux condition

$$\Phi_r(R, \theta, t) = 0 \quad \text{for} \quad 0 \leqslant \theta < 2\pi \tag{3}$$

is specified, where R is the radius of the cylinder.

For initial conditions, the surface potential $\Phi^{\mathrm{S}}(x, 0)$ and elevation $\eta(x, 0)$ are prescribed. This completes the initial-boundary-value problem for Φ. For computations, we impose periodic conditions far upstream and downstream, say at $x = \pm L$.

Following DY, we assume that Φ and η are $O(\epsilon)$ quantities, where ϵ, a small parameter, is a measure of the wave steepness. We then expand Φ in a perturbation series in ϵ up to order M:

$$\Phi(x, y, t) = \sum_{m=1}^{M} \Phi^{(m)}(x, y, t), \tag{4}$$

where $(\ )^{(m)}$ denotes a quantity of $O(\epsilon^m)$. We further expand each $\Phi^{(m)}$ evaluated on $y = \eta$ in a Taylor series about $y = 0$, so that

$$\Phi^S(x,t) \equiv \Phi(x,\eta,t) = \sum_{m=1}^{M} \sum_{l=0}^{M-m} \frac{\eta^l}{l!} \frac{\partial^l}{\partial y^l} \Phi^{(m)}(x,0,t). \tag{5}$$

The method we develop will, in principle, be able to account for nonlinearities up to an arbitrary order M in ϵ. In practice, however, (5) places a limit on the maximum steepness of the free surface we can consider. In particular, the validity and convergence of (5) is limited by the radius of convergence (from $y = 0$) of Φ, which cannot extend beyond the first singularity in the analytic continuation of Φ above $y = \eta$.

The nonlinear free-surface conditions (2) can be considered as evolution equations for Φ^S and η, provided that the surface vertical velocity $\Phi_y(x,\eta,t)$ can be obtained from the boundary-value problem. Thus, at a given instant of time, we can consider Φ^S and η known, and treat (5) as a Dirichlet boundary condition for the unknown Φ. Expanding (5) and collecting terms at each order, we obtain a sequence of boundary conditions for the unknown $\Phi^{(m)}$ on $y = 0$:

$$\Phi^{(m)}(x,0,t) = f^{(m)}, \quad m = 1,2,\ldots,M, \tag{6}$$

where
$$f^{(1)} = \Phi^S, \quad f^{(m)} = -\sum_{l=1}^{m-1} \frac{\eta^l}{l!} \frac{\partial^l}{\partial y^l} \Phi^{(m-l)}(x,0,t), \quad m = 2,3,\ldots,M. \tag{7}$$

The Dirichlet condition (6), in addition to $\Phi^{(m)}$ being periodic over $-L \leqslant x < L$, $\Phi_r^{(m)}(R,\theta,t) = 0$ for $0 \leqslant \theta < 2\pi$, and $\nabla\Phi^{(m)} \to 0$ as $y \to -\infty$, defines a sequence of boundary-value problems for $\Phi^{(m)}, m = 1,2,\ldots,M$, in the domain $y \leqslant 0$.

To solve for $\Phi^{(m)}$, we distribute dipoles $\mu^{(m)}(x,t)$ over the mean position of the free surface, and sources $\sigma^{(m)}(\theta,t)$ over the surface of the circular cylinder. Noting that $\mu^{(m)}$ and $\sigma^{(m)}$ are $2L$- and 2π-periodic in x and θ respectively, we expand them as Fourier series:

$$\mu^{(m)}(x,t) = \sum_{n=0}^{\infty} \mu_n^{(m)}(t)\, e^{in\pi x/L}, \qquad \sigma^{(m)}(\theta,t) = \sum_{n=0}^{\infty} \sigma_n^{(m)}(t)\, e^{in\theta}, \tag{8}$$

where real parts of the complex quantities are implied. The unknown perturbation potential $\Phi^{(m)}$ is then given in terms of the modal amplitudes $\mu_n^{(m)}(t)$ and $\sigma_n^{(m)}(t)$:

$$\Phi^{(m)}(x,y,t) = \sum_{n=0}^{\infty} \mu_n^{(m)}(t)\, \Psi_{Fn}(x,y) + \sum_{n=0}^{\infty} \sigma_n^{(m)}(t)\, \Psi_{Bn}(x,y), \tag{9}$$

where Ψ_{Fn} and Ψ_{Bn} are influence functions of the nth mode dipole and source distributions on the free surface and body respectively. These influence functions are given in terms of the Fourier integrals:

$$\Psi_{Fn}(x,y) = \int_{-L}^{L} e^{in\pi x'/L} G_{y'}(x,y;x',0)\, dx', \tag{10a}$$

$$\Psi_{Bn}(x,y) = \int_{0}^{2\pi} e^{in\theta'} G(r,\theta;R,\theta')\, R\, d\theta', \tag{10b}$$

where $G(x,y;x',y')$ is the $2L$-periodic source potential in two dimensions:

$$G(x,y;x',y') = \tfrac{1}{2}\log\left[\sin^2\left(\frac{x-x'}{2L/\pi}\right) + \sinh^2\left(\frac{y-y'}{2L/\pi}\right)\right]. \tag{11}$$

With this construction, (9) satisfies Laplace's equation and all the boundary conditions with the exception of those on the mean free surface and the body. Substituting (9) into (3) and (6) for each order, the modal amplitudes $\mu_n^{(m)}(t)$ and $\sigma_n^{(m)}(t)$ are determined successively for $m = 1, \ldots, M$, in terms of $\Phi^{(m)}(x, 0, t)$, which ultimately is given by the known $\Phi^{\mathrm{S}}(x, t)$ and $\eta(x, t)$ according to (7).

After the boundary-value problems for $\Phi^{(m)}$ are solved up to the desired order M, the vertical velocity on the free surface is given by

$$\Phi_y(x, \eta, t) = \sum_{m=1}^{M} \sum_{l=0}^{M-m} \frac{\eta^l}{l!} \frac{\partial^{l+1}}{\partial y^{l+1}} \Phi^{(m)}(x, 0, t). \tag{12}$$

The vertical derivatives here (and in (7)) are obtained in terms of the modal amplitudes:

$$\Phi_y^{(m)}(x, 0, t) = \sum_{n=0}^{\infty} \mu_n^{(m)}(t) \frac{\partial}{\partial y} \Psi_{\mathrm{F}n}(x, 0) + \sum_{n=0}^{\infty} \sigma_n^{(m)}(t) \frac{\partial}{\partial y} \Psi_{\mathrm{B}n}(x, 0). \tag{13}$$

Thereafter, higher derivatives are found by using Laplace's equation (e.g. $\Phi_{yy}^{(m)} = -\Phi_{xx}^{(m)}$, $\Phi_{yyy}^{(m)} = -(\phi_y^{(m)})_{xx}, \ldots$), and the x-derivatives are easily evaluated in the Fourier space. The evolution equations (2) can then be integrated for the new values of Φ^{S} and η. The process is repeated starting from initial conditions.

The potential on the body is available from (9), and the pressure on the cylinder can be evaluated according to Bernoulli's equation:

$$\frac{P(\theta, t)}{\rho} = -\frac{\partial}{\partial t} \sum_{m=1}^{M} \Phi^{(m)}(R, \theta, t) - \frac{1}{2R^2} \left[\frac{\partial}{\partial \theta} \sum_{m=1}^{M} \Phi^{(m)}(R, \theta, t) \right]^2, \tag{14}$$

where ρ is the fluid density. The instantaneous force on the body is obtained by direct integration of (14).

3. Numerical method

3.1. *Implementation*

The time simulation of the nonlinear wave–body problem up to an arbitrary order M consists of three main steps. Beginning from initial values for Φ^{S} and η, at each successive time step: (i) solve the boundary-value problem for the perturbation velocity potentials $\Phi^{(m)}(x, y, t), m = 1, \ldots, M$; (ii) evaluate the vertical velocity at the free surface $\Phi_y(x, \eta, t)$; and (iii) integrate the evolution equations (2) forward for $\Phi^{\mathrm{S}}(x, t + \Delta t)$ and $\eta(x, t + \Delta t)$; and the process is repeated.

In practice, the numbers of Fourier modes for the dipole and source distributions are truncated at some suitable numbers, say, N_{F} for $\mu^{(m)}$ and N_{B} for $\sigma^{(m)}$. Note that since $\mu^{(m)}$ and $\sigma^{(m)}$ are in general smooth periodic functions of x and θ respectively, the convergence of (8) with N_{F} and N_{B} is exponentially rapid, as is demonstrated in §3.3. Given the boundary-value problems for $\Phi^{(m)}, m = 1, \ldots, M$, the modal amplitudes $\mu_n^{(m)}(t)$, $n = 0, \ldots, N_{\mathrm{F}}$, and $\sigma_n^{(m)}(t), n = 0, \ldots, N_{\mathrm{B}}$, are determined by satisfying the Dirichlet and Neumann conditions at N_{F} and N_{B} equally spaced control points on the mean free surface and body respectively. The resulting $N_{\mathrm{F}} + N_{\mathrm{B}}$ linear equations can be formally represented as

$$\left.\begin{aligned} [C_{\mu\mu}]\{\mu^{(m)}\} + [C_{\mu\sigma}]\{\sigma^{(m)}\} &= \{f^{(m)}\}, \\ [C_{\sigma\mu}]\{\mu^{(m)}\} + [C_{\sigma\sigma}]\{\sigma^{(m)}\} &= 0, \end{aligned}\right\} \tag{15}$$

where $[C_{\mu\mu}]$, $[C_{\mu\sigma}]$, $[C_{\sigma\mu}]$, and $[C_{\sigma\sigma}]$ are respectively the $N_F \times N_F$, $N_F \times N_B$, $N_B \times N_F$, and $N_B \times N_B$ modal influence matrices given in terms of the basis functions; and $\{\mu^{(m)}\}$, $\{\sigma^{(m)}\}$, the vectors of the unknown modal amplitudes $\mu_n^{(m)}, n = 0, \ldots, N_F$, and $\sigma_n^{(m)}$, $n = 0, \ldots, N_B$. Solving these equations, we obtain, again formally,

$$\begin{aligned} \{\sigma^{(m)}\} &= [T_{\sigma f}]\{f^{(m)}\}, \\ \{\mu^{(m)}\} &= [T_{\mu f}]\{f^{(m)}\} + [T_{\mu\sigma}]\{\sigma^{(m)}\}, \end{aligned} \tag{16}$$

where $[T_{\sigma f}](N_B \times N_F)$, $[T_{\mu f}](N_F \times N_F)$, and $[T_{\mu\sigma}](N_F \times N_B)$, are related to the inverses of the influence matrices in (15).

Once $\{\mu^{(m)}\}$ and $\{\sigma^{(m)}\}$ are obtained, the perturbation vertical velocities at the control points on the free surface follow from (13), which take the form

$$\{\Phi_y^{(m)}\} = [W_\mu]\{\mu^{(m)}\} + [W_\sigma]\{\sigma^{(m)}\}, \tag{17}$$

where $[W_\mu](N_F \times N_F)$, and $[W_\sigma](N_F \times N_B)$ are known matrices given by (13) in terms of the basis functions.

In practice, the boundary-value problems are solved using a pseudospectral approach, wherein all the spatial derivatives are evaluated in the spectral representation, while nonlinear products (such as those in (7)) are computed in physical space at the discrete control points. The rapid transformations between the representations are affected by fast-Fourier transforms (FFTs).

It is important to note that in the present high-order method, the $[T]$ and $[W]$ matrices in (16) and (17) are functions of the mean geometry only. For the diffraction problem, then, they are independent of time and need to be evaluated only once for the entire simulation. More significantly, since for typical applications (especially for three-dimensional problems) $N_F \gg N_B$ in the spectral approach, the $N_F \times N_F$ matrices $[T_{\mu f}]$ and $[W_\mu]$ need not be explicitly realized as the contributions $[T_{\mu f}]\{f^{(m)}\}$ and $[W_\mu]\{\mu^{(m)}\}$ can be evaluated in $O(N_F \ln N_F)$ operations via FFT. Consequently, the net computational effort is approximately proportional to N_F and not N_F^2. Specifically, the total operational count of the method is $[O(MN_F \ln N_F) + O(MN_F N_B)]$ per time step, with an initial set-up effort of $[O(N_B^2 N_F) + O(N_B N_F \ln N_F)]$.

With the surface vertical velocities thus obtained from (17) and (12), the nonlinear evolution equations (2) can be integrated as a coupled set of nonlinear ODEs. We employ the fourth-order Runge–Kutta scheme which requires twice as many evaluations as the commonly used multi-step predictor–corrector (e.g. the Adams–Bashforth–Moulton) methods of the same order but has a somewhat lower global truncation error and a larger stability region (see e.g. Dommermuth *et al.* 1988).

For the diffraction problem, we choose as initial conditions exact deep-water Stokes waves of steepness $\epsilon = kA$ ($2A \equiv \eta_{\max} - \eta_{\min}$), wavelength $\lambda = 2L/N_w$, i.e. N_w complete waves in the periodic domain $[-L, L]$, and period T. To calculate the initial values $\eta(x, 0)$ and $\Phi^S(x, 0)$, we follow Schwartz (1974), but solve the mapping (Schwartz' equation 2.6) by direct numerical iterations.

3.2. *Error considerations*

The main sources of computational error for the present high-order wave–body simulations are: (i) errors due to truncation in the numbers of Fourier modes N_F, N_B, and the perturbation order M; (ii) error due to the finite (periodic) computational domain for a given simulation time, T_S; (iii) amplification of round-off and truncation errors; (iv) aliasing errors of the pseudospectral method; (v) errors due to numerical time integration; and (vi) for estimates of mean and harmonic force coefficients etc., errors due to the finite simulation time, T_S, of the initial-value problem.

Errors due to truncation of modes N_F, N_B, and order M

For sufficiently smooth η and Φ^S, the numerical errors in the Fourier representations of η, Φ^S, $\mu^{(m)}$ and $\sigma^{(m)}$ vanish exponentially as N_F and $N_B \to \infty$. Similarly, for mild nonlinearities, the truncation error after order M is $O(\epsilon^{M+1})$, and the convergence is exponential with increasing M. As pointed out after (5), such convergence ceases beyond a certain wave steepness. For regular Stokes waves, the maximum wave steepness for exponential convergence of the method is found to be $\epsilon = kA \sim 0.35$ (see DY table 1). The corresponding maximum local slope is $\epsilon_L \equiv (\partial\eta/\partial x)_{max} \sim 0.38$. In the presence of a submerged body, the incident Stokes wave steepness ϵ is neither the limiting nor useful parameter due to local wave steepening over the body. Using ϵ_L instead, our present calculations with a body confirm the result of DY based on Stokes waves. It is important to point out that converged results (not necessarily exponentially fast) for large local slopes up to $\epsilon_L \sim 1.5$ can and have been obtained in the present simulations (see also DY figures 2 and 5).

Error due to the finite computational domain

For a computational domain fixed relative to wavelength and body dimension, the solution in the near field of the body will eventually be distorted due to 'reflections' from the periodic boundaries as the simulation time T_S is increased. This error is avoided by successively increasing the length of the periodic domain (increasing N_w keeping kA, kR and kH constant) until the quantities of interest no longer vary (see §3.3). We remark that with the $O(N_F)$ efficiency of the present method, the computation cost increases only linearly with N_w.

Amplification of round-off and truncation errors

In any computational model without dissipation, nonlinear interactions cause energy in the lower modes to cascade to higher modes which eventually accumulates at the highest wavenumbers retained in the model. As pointed out in DY, this is accompanied by an amplification of numerical error in the modal amplitudes which increases with the mode number. This combined effect is the root cause of large-wavenumber instabilities in our nonlinear simulations. To avoid such instabilities, we follow DY and apply an ideal numerical low-pass filter in the Fourier space:

$$\Lambda_I(n,\alpha) = \begin{cases} 1 & \text{for} \quad n \leqslant \alpha N_F \\ 0 & \text{for} \quad n > \alpha N_F \end{cases}. \tag{18}$$

Typically, we apply Λ_I with $\alpha = 0.8$ to the spectra of η and Φ^S every five time steps.

Aliasing errors

In a pseudospectral approach, the product $h = \boldsymbol{f}\cdot\boldsymbol{g}$, represented respectively by Fourier modes $h_n, f_n, g_n, n \leqslant N$, is performed in physical space at equally spaced points. This results in aliasing errors due to the finite Fourier representations. It is well known that the best approximation (in the mean-square sense) to the product is the so-called alias-free sum (e.g. Orszag 1971). To obtain this, we double the number of Fourier modes and the number of collocation points to $2N$, calculate the product $H = FG$, as before in physical space, where $(F_n, G_n) = (f_n, g_n)$ for $|n| \leqslant N$ and $(F_n, G_n) = (0,0)$ for $N < |n| \leqslant 2N$, and define the alias-free product, h, by $h_n = H_n$ for $|n| \leqslant N$. For products involving two or more terms, the multiplication is done successively, where each factor is made alias-free before multiplying by the next term.

N_w	$M=2$	$M=3$	$M=4$
8	−1.0650	−1.0750	−1.0800
16	−1.0784	−1.0876	−1.0907
32	−1.0800	−1.0890	−1.0920

TABLE 1. Convergence of the normalized horizontal drift force, $\bar{F}_x/\rho g A^2\epsilon^2$, on a submerged circular cylinder with increasing number of wavelengths N_w of the periodic domain and for different order M. $kA = 0.04$, $kR = 0.4$, $H/R = 2$; and $N_F = 64N_w$, $N_B = 256$, $T/\Delta t = 64$, $\tau_0 = 5T$.

N_B	$M=2$	$M=3$	$M=4$
64	−1.0656	−1.0845	−1.0880
128	−1.0778	−1.0869	−1.0900
256	−1.0784	−1.0876	−1.0907

TABLE 2. Convergence of the normalized horizontal drift force, $\bar{F}_x/\rho g A^2\epsilon^2$, on a submerged circular cylinder with increasing number of body modes N_B and order M. $kA = 0.04$, $kR = 0.4$, $H/R = 2$; and $N_w = 16$, $N_F = 64N_w$, $T/\Delta t = 64$, $\tau_0 = 5T$.

Errors due to numerical time integration

The fourth-order Runge–Kutta scheme we use is conditionally stable for the linearized equation for $g\kappa_{\max}\Delta t^2 \leqslant 8$, where $\kappa_{\max}$ is the maximum grid (Nyquist) wavenumber. This should be a necessary condition for the nonlinear problem. The local truncation error of the fourth-order Runge–Kutta is $O(\Delta t^5)$, so that the global truncation error for $T_S = O(1)$ is fourth-order in Δt.

Errors in the estimation of mean and limit-cycle force coefficients

One of the main interests of this study is the mean drift force on the cylinder. To obtain this from the initial-value simulation, we define for definiteness

$$\bar{F}(\tau_0) = \frac{1}{T}\int_{\tau_0}^{\tau_0+T} F(t)\,\mathrm{d}t, \tag{19}$$

where $F(t)$ is the time-dependent force on the cylinder, T the fundamental period (of the incident wave), and τ_0 a time interval selected so that limit-cycle values are obtained. The (rapid) convergence of $\bar{F}$ with τ_0 is an important and desired property.

3.3. *Numerical convergence tests*

Systematic tests are performed to verify the accuracy and convergence of the present method. For specificity, we consider only the horizontal (mean) drift force $\bar{F}_x$ on the submerged circular cylinder. This offers a severe test on the accuracy of the high-order method since the horizontal drift force is zero up to second order (Ogilvie 1963) and its magnitude is (at most) fourth order in the incident wave steepness.

Table 1 shows the results for the horizontal drift force for increasing N_w, keeping kA, kR and kH fixed. For $N_w = 16$, $\bar{F}_x$ shows convergence up to three significant figures. The convergence with number of body modes, N_B, keeping N_F and other parameters fixed, is shown in table 2. For a given order M, $\bar{F}_x$ converges to its limit exponentially fast as N_B is increased, although N_B needs to be sufficiently large for the exponential convergence with M to take place. Similar rapid convergence with respect to the number of free-surface modes, N_F, and with order M is displayed in

ϵ	N_F/N_w	$M=2$	$M=3$	$M=4$
0.04	32	−1.0479	−1.0520	−1.0550
	64	−1.0784	−1.0876	−1.0907
	128	−1.0804	−1.0898	−1.0930
0.08	32	−0.9399	−0.9617	−0.9717
	64	−1.0083	−1.0435	−1.0561
	128	−1.0072	−1.0432	−1.0588
0.12	32	−0.8276	−0.8713	−0.8885
	64	−0.8977	−0.9722	−1.0079
	128	−0.9102	−0.9643	−0.9910
0.16	32	−0.7365	−0.8152	−0.8427
	64	−0.7512	−0.8620	−0.9438

TABLE 3. Convergence of the normalized horizontal drift force, $\bar{F}_x/\rho g A^2\epsilon^2$, on a submerged circular cylinder with number of free-surface modes N_F and order M for different incident wave slopes $\epsilon = kA$. $kR = 0.4$, $H/R = 2$; and $N_w = 16$, $N_B = 256$, $T/\Delta t = 64$, $\tau_0 = 5T$.

τ_0/T	$M=2$	$M=3$	$M=4$
0	−5.8477	−5.9392	−5.9414
1	−0.9742	−0.9811	−0.9821
2	−1.0724	−1.0847	−1.0869
3	−1.0877	−1.0919	−1.0941
4	−1.0662	−1.0916	−1.0926
5	−1.0784	−1.0876	−1.0907

TABLE 4. Convergence of the normalized horizontal drift force, $\bar{F}_x/\rho g A^2\epsilon^2$, on a submerged circular cylinder with duration of simulation τ_0 and order M. $kA = 0.04$, $kR = 0.4$, $H/R = 2$; and $N_w = 16$, $N_F = 64N_w$, $N_B = 256$, $T/\Delta t = 64$.

$T/\Delta t$	$M=2$	$M=3$	$M=4$
32	−1.0766	−1.0862	−1.0893
48	−1.0775	−1.0868	−1.0900
64	−1.0784	−1.0876	−1.0907

TABLE 5. Convergence of the normalized horizontal drift force, $\bar{F}_x/\rho g A^2\epsilon^2$, on a submerged circular cylinder with integration time step Δt and order M. $kA = 0.04$, $kR = 0.4$, $H/R = 2$; and $N_w = 16$, $N_F = 64N_w$, $N_B = 256$, $\tau_0 = 5T$.

table 3 for a range of incident wave steepness, $\epsilon = kA$. Again, the exponential convergence with N_F is achieved for any M, while that with M requires first that N_F is adequately large. When the maximum local slope, ϵ_L, of the free surface (typically above the cylinder) exceeds ~ 0.4, however, the convergence becomes only algebraic. This has occurred, for example, for the case of $\epsilon = 0.16$ in table 3.

We next show the approach to the steady-state limit (limit-cycle) of the forces on the cylinder by considering the convergence of (19) with τ_0. This is shown in table 4 for different order M. The steady-state limit is reached rapidly after $\tau_0 \sim 2T$. Finally, we show the convergence of the numerical time integration with Δt in table 5. The expected $O(\Delta t/T)^4$ global error is obtained provided that the solution to the boundary-value problem itself is sufficiently accurate.

Unless otherwise stated, for all subsequent computations, we use $N_w = 16$, $N_F = 64N_w$, $N_B = 256$, $\tau_0 = 5T$, and $\Delta t = T/64$. Based on the foregoing numerical tests, we anticipate the maximum error for $\bar{F}_x$ to be less than 1%.

In addition to these convergence tests, all our computations are checked for the conservation of volume, $\int_L^{-L} \eta \, dx$, or alternatively the vanishing of the volume flux, $\int_{-L}^{L} \eta_t \, dx$ (with η_t given directly by (2a)); as well as the invariance of the total energy:

$$\int_{S_F} \Phi^S \Phi_n^S \, ds + \int_{-L}^{L} \eta^2 \, dx, \tag{20}$$

where Φ_n^S is the normal velocity on the free surface S_F, and the first and second terms are proportional respectively to the kinetic and potential energies. For all later results we present, the volume flux is within $\sim 10^{-5}$, and the volume and total energy do not deviate by more than 1% from their initial values.

The force on the cylinder can also be obtained by applying the momentum theorem:

$$\frac{\boldsymbol{F}}{\rho} = -\int_0^{2\pi} \Phi_t \boldsymbol{n} R \, d\theta - \frac{d}{dt} \int_{S_F} \Phi \boldsymbol{n} \, ds, \tag{21}$$

where the unit normal vector $\boldsymbol{n}$ is positive out of the fluid. In all cases, the force from (21) compares well with that obtained by direct integration of the pressure (14) over the body surface. For the fourth-order horizontal drift force in §4.4, for example, the difference between the two is always less than 1%.

4. Numerical results

We consider the diffraction of Stokes waves by a fixed, submerged circular cylinder. To facilitate comparisons to existing frequency-domain results, we first make explicit the relationships between the harmonic amplitudes obtained using the present high-order time-domain approach and those resulting from direct perturbation methods in the frequency domain. We then present results for the high-order diffracted wave amplitudes, the oscillatory force coefficients, and finally the mean forces on the cylinder. Comparisons to theoretical, computational and experimental results are made whenever they are available.

4.1. *Relation to frequency-domain perturbation results*

Although the present approach is strictly a time-domain (initial-value problem) one, and steady and harmonic amplitudes are obtained via harmonic analysis of the limit-cycle time histories, these results can be related in a direct way to the linear and higher-order components of perturbation methods in the frequency domain. In a typical frequency-domain approach, the time dependence is factored out explicitly and the velocity potential written as

$$\Phi = \sum_{n=0}^{\infty} \mathrm{Re}\,(\tilde{\phi}_n \, e^{in\omega t}), \tag{22}$$

where $\omega = 2\pi/T$. Each $\tilde{\phi}_n$ is then expanded in a perturbation series in the wave steepness, ϵ:

$$\tilde{\phi}_n = \sum_{m=1}^{\infty} \epsilon^m \tilde{\phi}_n^{(m)}, \tag{23}$$

and the boundary-value problems for $\tilde{\phi}_n^{(m)}$ are solved.

In the present method, the initial-boundary-value problem for $\Phi(\boldsymbol{x}, t)$ is integrated

	Ogilvie (1963)	Vada (1987)	Present results
$F_{x1}/\rho gRA$	1.15	1.15	1.1406 ($M = 1$)
$F_{x2}/\rho gA^2$	—	0.28	0.2754 ($M = 2$)
T_2/kA	—	2.65	2.7025 ($M = 2$)

TABLE 6. Comparisons between existing frequency-domain and the present time-domain results for the (normalized) first- and second-harmonic horizontal force and the second-harmonic transmission coefficients. $kR = 0.4$, $H/R = 2$ and $kA = 0.08$.

accurately to the specified order M in ϵ. Despite the truncation at M (cf. (4), (5)), the presence of the nonlinear terms in (2) eventually causes all time harmonics to be present in Φ, in fact in each $\Phi^{(m)}$. Upon reaching limit cycle, the (complex) amplitudes of these harmonics are then extracted via Fourier decomposition:

$$\phi_n^{(m)} = \frac{1}{T}\int_{\tau_0}^{\tau_0+T} \Phi^{(m)}(t)\,\mathrm{e}^{-\mathrm{i}n\omega t}\,\mathrm{d}t, \quad n = 1,2,\ldots; \quad m = 1,2,\ldots,M. \tag{24}$$

It should be pointed out that, in general, $\phi_n^{(m)}, n > m$ (and also $n = 0, m = 1$), are small as expected but do not vanish. In the high-order time-domain approach, there is no direct relationship between mth-order terms in (24) and those in (23) (cf. (7)). For direct comparisons then, it is useful to define the amplitude:

$$\phi_n^{\langle M\rangle} = \sum_{m=1}^{M} \phi_n^{(m)}, \quad n = 1,2,\ldots, \tag{25}$$

where M is the order of the simulation. Note that the magnitude of $\phi_n^{\langle M\rangle}$ is $O(\epsilon^n)$, except for $\phi_0^{\langle M\rangle}$ which is of second order. With this notation, then, the amplitudes in (23) and (25) are related by

$$\tilde{\phi}_0^{(2)} = \phi_0^{\langle 2\rangle} + O(\epsilon^3), \tag{26a}$$

$$\tilde{\phi}_n^{(n)} = \phi_n^{\langle M\rangle} + O(\epsilon^{n+1}), \quad n > 0, \text{ and } M \geqslant n, \tag{26b}$$

while such simple relationships cannot, in general, be written for the amplitudes in (24). Similar formulae and results apply also to other quantities such as forces, wave amplitudes, etc. We remark finally that, in some sense, the present results are more 'physical' in that they correspond directly to what one might measure in a laboratory.

To illustrate the relationship between the present time-domain and existing frequency-domain results, we show in table 6 the correspondences (26) for the normalized harmonic forces and transmission coefficient. The frequency-domain values are taken from Ogilvie (1963) (first order) and Vada (1987) (second order). It is verified that the discrepancies are indeed of $O(\epsilon)$ or less.

4.2. *Diffracted waves*

For the diffraction of waves by a submerged circular cylinder in deep water, Dean (1948) and Ursell (1950) show that the linear potential produces no reflected waves and all incoming waves are transmitted downstream. This is confirmed experimentally by Chaplin (1984), suggesting further that the reflected waves may be small even to higher order. Recently, Palm (1991) proves analytically that the

	$n=M=1$	$n=M=2$	$n=M=3$
$R_n^{\langle M\rangle}$	0.0250	0.0025	0.0003

TABLE 7. Harmonic amplitudes of the reflection coefficient for the diffraction of Stokes waves by a submerged circular cylinder, $kA = 0.05$, $kR = 0.4$ and $H/R = 2$. The numerical parameters are $N_w = 16$, $N_F = 64N_w$, $N_B = 256$, $T/\Delta t = 64$, and $\tau_0 = 9T$.

leading-order part (at order m) of wave mode of frequency $m\omega$ is not reflected. For the transmitted wave, however, experiments by Grue (1991) show that the amplitudes are significantly affected by the nonlinear interactions between the cylinder and the free surface. Here we compare the high-order spectral method predictions of the reflected and transmitted wave amplitudes to these analytical and experimental results.

Expecting the reflected wave amplitude to be at most $O(\epsilon^2)$, we write the free-surface elevation far upstream of the cylinder as

$$\eta(x,t) = a_1\cos(kx-\omega t)+\tfrac{1}{2}ka_1^2\cos 2(kx-\omega t)+\tfrac{3}{8}k^2a_1^3\cos 3(kx-\omega t)$$
$$+a_1'\cos(kx+\omega t+\delta_1')+a_2'\cos(4kx+2\omega t+\delta_2')+a_3'\cos(9kx+3\omega t+\delta_3')$$
$$+O(\epsilon^4), \quad x<0. \tag{27}$$

Similarly, far downstream we write

$$\eta(x,t) = b_1\cos(kx-\omega t+\delta_1)+\tfrac{1}{2}kb_1^2\cos 2(kx-\omega t+\delta_1)+\tfrac{3}{8}k^2b_1^3\cos 3(kx-\omega t+\delta_1)$$
$$+b_2\cos(4kx-2\omega t+\delta_2)+b_3\cos(9kx-3\omega t+\delta_3)+O(\epsilon^4), \quad x>0. \tag{28}$$

The reflection and transmission coefficients for each harmonic are defined accordingly by $R_1 = a_1'/a_1, R_2 = a_2'/a_1, R_3 = a_3'/a_1$, and $T_1 = b_1/a_1, T_2 = b_2/a_1, T_3 = b_3/a_1$, etc.

In numerical simulations, we record the time series of the free-surface elevation at a location far upstream (at $x = -8R$), and another far downstream ($x = 8R$), the latter corresponding to the measurement position of Grue (1991). At these positions, the limit cycle for the surface elevation up to third harmonics is approached after typically $\tau_0/T \sim 7$–8. (The simulations themselves are typically stopped after $\sim 10T$ before any appreciable effects due to images of the periodic boundaries are felt.) The harmonic amplitudes of the transmitted and reflected waves are then obtained via Fourier analysis of the limit-cycle time histories at these two locations.

To study the effect of nonlinearity on wave reflection and transmission, we first fix $kR = 0.4$ and $kH = 0.6$, and consider the dependence of R_n and T_n on the incident wave slope kA. For the reflected wave amplitudes, the dominant contribution for each $n > 0$ harmonic is at order $m = n$, i.e. $R_n^{(n)}$. In view of (26), this can be estimated to leading order by $R_n^{\langle n\rangle}$. Table 7 shows a typical example for $kA = 0.05$. It is seen that $R_n^{\langle n\rangle}, n = 1,2,3$, is at most of $O(\epsilon^n)$ and is at least one order higher than the transmission coefficients (which are $O(1)$). These (limited) results provide a direct numerical confirmation of the analytical predictions of Palm (1991).

The dependence of the first-harmonic transmission coefficient, T_1, on incident wave steepness $\epsilon = kA$ is shown in figure 1. For linear theory, $T_1 \equiv 1$ and is not a function of ϵ. However, the measurements of Grue (1991) show that T_1 in fact decreases appreciably from 1 as ϵ increases. Our converged numerical results confirm this nonlinear dependence quantitatively up to $\epsilon \sim 0.08$. (Beyond $\epsilon \sim 0.08$, extensive

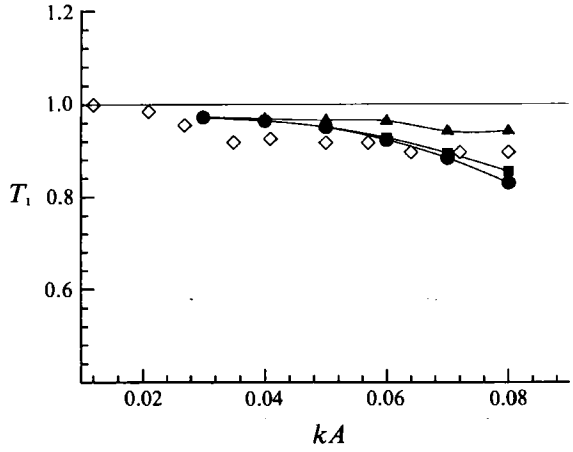

FIGURE 1. Dependence of the first-harmonic wave transmission coefficient T_1 on the incident wave slope kA. Experiments (Grue 1991) (◇); linear solution (——); and present high-order results for $M = 2$ (▲), $M = 3$ (■), and $M = 4$ (●). ($kR = 0.4$, $H/R = 1.5$.)

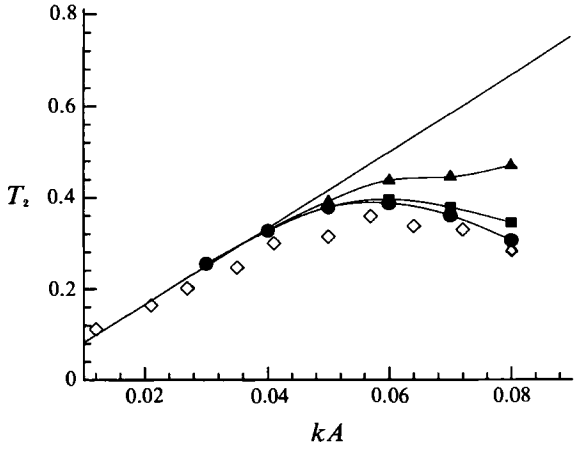

FIGURE 2. Dependence of the second-harmonic wave transmission coefficient T_2 on the incident wave slope kA. Experiments (Grue 1991) (◇); second-order computation (Vada 1987) (——); and present high-order results for $M = 2$ (▲), $M =$ (■), and $M = 4$ (●). ($kR = 0.4$, $H/R = 1.5$.)

wave breaking over the cylinder is reported by Grue 1991. For clarity, these experimental data points are omitted from this and subsequent figures.) From figure 1, we also conclude that it is necessary to include third-order ($M = 3$) contributions to correctly account for the behaviour of T_1.

Figure 2 shows comparisons for the second-harmonic transmission coefficient T_2 among our high-order numerical results, Vada's (1987) second-order frequency-domain computations, and Grue's (1991) experimental data. The strong nonlinear interactions over the cylinder result in a significant reduction of T_2 from the second-order perturbation result (which predicts a linear dependence on ϵ). Although our numerical results show some indication of convergence at $M = 4$, comparison to the measured data indicates that even higher-order effects are present in T_2 for near-breaking conditions.

Figure 3 summarizes the dependence of transmitted wave amplitudes on $\epsilon = kA$

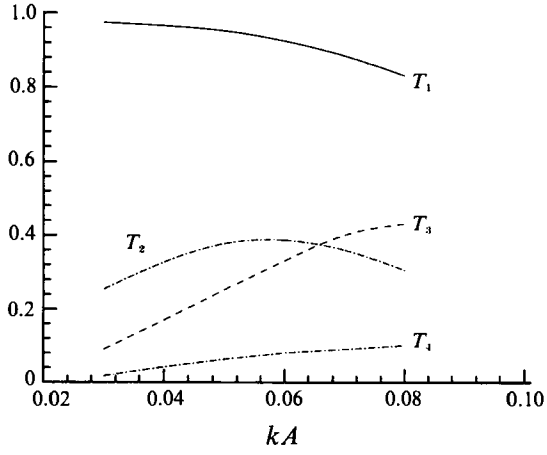

FIGURE 3. High-order spectral solution ($M = 4$) of harmonic wave transmission coefficients T_1, T_2, T_3, T_4 as a function of incident wave slope kA. ($kR = 0.4$, $H/R = 1.5$.)

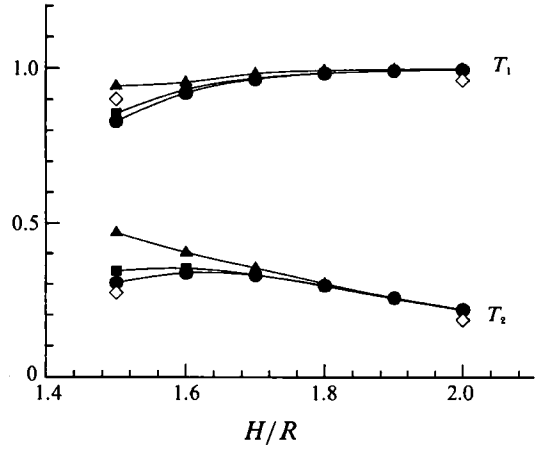

FIGURE 4. Dependence of the first- and second-harmonic wave transmission coefficients on the body submergence H/R. Experiments (Grue 1991) (◇); and present high-order results for $M = 2$ (▲), $M = 3$ (■), and $M = 4$ (●). ($kR = 0.4$, $kA = 0.08$.)

for this case ($kR = 0.4, kH = 0.6$). Also shown are our predictions for T_3 and T_4 which have been obtained for the first time. It is interesting to note that as ϵ increases beyond ~ 0.055, T_2 decreases while T_3 continues to grow, so that for steep waves ($\epsilon > \sim 0.065$) T_3 becomes greater than T_2. A direct experimental confirmation for these very high harmonics, however, may be difficult and has not yet been obtained. We caution that the present results for T_3 and T_4 have been obtained up to $M = 4$ only. Although the dominant components are included, higher values of M may lead to some reductions of their amplitudes (cf. figure 2).

Finally, we study the dependence of T_n on the body submergence H/R by fixing $kR = 0.4, kA = 0.08$ and consider varying kH. The numerical results for T_1 and T_2 are shown in figure 4. For this case, two experimental points at $H/R = 1.5$ and 2 are available from Grue (1991). For large H/R, T_1 approaches 1 rapidly, while T_2 decreases monotonically. The coefficients are overpredicted by these asymptotes, however, as the cylinder approaches the surface and nonlinear effects evidently

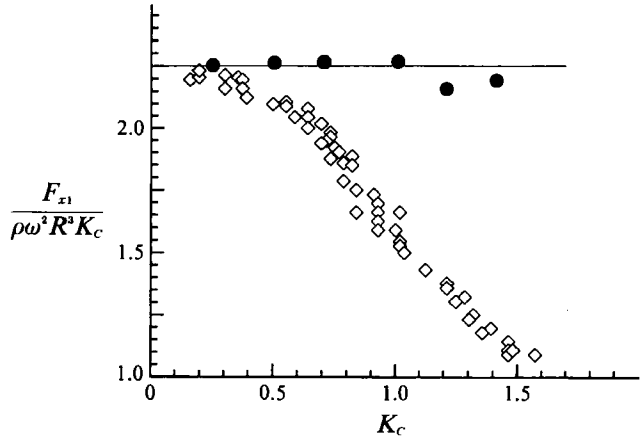

FIGURE 5. The first-harmonic horizontal force F_{x1} as a function of Keulegen–Carpenter number K_C. Experiments (Chaplin 1984) (◇); linear result (Ogilvie 1963) (——); and present high-order results for $M = 4$ (●). ($kR = 0.21$, $H/R = 2.0$.)

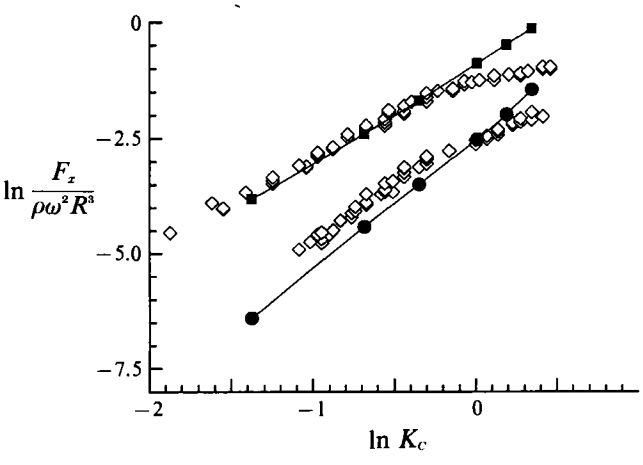

FIGURE 6. The second- and third-harmonic horizontal forces F_{x2}, F_{x3} as a function of Keulegen–Carpenter number K_C. Experiments (Chaplin 1984) (◇); and present high-order results with $M = 4$ for F_{x2} (■) and F_{x3} (●). ($kR = 0.21$, $H/R = 2.0$.)

become important. This is seen from the differences among the results for $M = 2$, 3, and 4. Indeed, comparison with experimental data suggests that even higher-order interactions play a role.

4.3. *Oscillating forces*

As demonstrated in table 4, the limit cycle for the force time history is reached rapidly after $\tau_0/T \sim 3$. The amplitudes of the force harmonics are then obtained using Fourier analysis (with $\tau_0/T = 5$).

Figure 5 shows comparisons for the first-harmonic horizontal force amplitude F_{x1} among our high-order ($M = 4$) numerical results, linear (potential flow) analytic solution (Ogilvie 1963), and experimental measurements of Chaplin (1984). Following Chaplin, we plot F_{x1} here as a function of the Keulegan–Carpenter number defined as $K_C = \pi e^{-kH}A/R$, which is based on linear deep-water waves. Comparing just the theoretical and computed results, it is remarkable that the first-harmonic amplitude is affected very little by nonlinear effects at least up to $K_C \sim 1$. On the other hand,

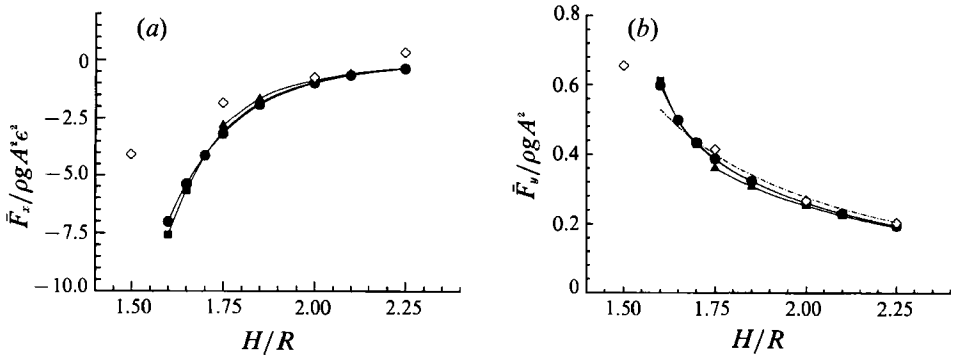

FIGURE 7. (*a*) Horizontal and (*b*) vertical drift forces as functions of body submergence. Experiments (Miyata *et al.* 1988) (◇); linear potential solution (Ogilvie 1963) (—·—); and present high-order results for $M = 2$ (▲), $M = 3$ (■), and $M = 4$ (●). ($kR = 0.4$, $\epsilon = kA = 0.12$.)

as suggested by Chaplin, effects of (clockwise) circulation around the cylinder result in a sharp decrease of F_{x1} for $K_C > \sim 0.5$ (possible effects of flow separation and wave breaking also cannot be ruled out). Our numerical results also show a reduction due to nonlinear diffraction but the magnitude is small compared to that due to circulation or real fluid effects.

In direct contrast to the first-harmonic force, circulation does not appear to affect the higher-harmonic forces as shown in figure 6 for F_{x2} and F_{x3}. The higher-order (potential flow) results are in excellent agreement with Chaplin's data up to $K_C \sim 1$, beyond which the effects of wave breaking most likely are important. The computed data also readily confirm the expected quadratic and cubic dependencies respectively of F_{x2} and F_{x3} on the Keulegan–Carpenter number.

4.4. *Mean forces*

We finally turn to the steady (drift) force on the cylinder which is the main focus of this study. First, we show the dependence of mean forces on body submergence by varying kH with fixed $kR = 0.4$ and $kA = 0.12$. This is shown in figure 7 where our high-order calculations using $M = 2, 3, 4$ are compared with the measurements of Miyata *et al.* (1988). The horizontal drift force $\bar{F}_x$, figure 7 (*a*), is negative (against the direction of wave propagation) with a magnitude which increases, as expected, with decreasing submergence. Except for relatively shallow submergence, $H/R < \sim 1.75$, the numerical predictions agree well with measurements. Since our computations do not account for wave breaking, it is evident that nonlinear diffraction effect rather than wave breaking is the dominant cause of the negative drift force. For $H/R < \sim 1.75$, extensive wave breaking is observed in the experiments, and the magnitude of the negative drift force is smaller compared to the diffraction results. This provides some evidence that the presence of wave breaking may lead to positive mean horizontal force on the cylinder.

For the mean uplift force $\bar{F}_y$, figure 7 (*b*), our numerical results compare well with both the second-order analytic solution (Ogilvie 1963) and the measurements of Miyata *et al.* (1988). Higher-order interactions and wave breaking effects are evidently less important for the vertical mean force.

It is clear that since $\bar{F}_x = 0$ up to second order in wave steepness (Ogilvie 1963), the next available contribution is at most fourth order. Likewise, one may expect a fourth-order correction to the second-order $\bar{F}_y$. These expectations are confirmed by our calculation of the mean forces for varying incident wave slopes kA (fixing $kR =$

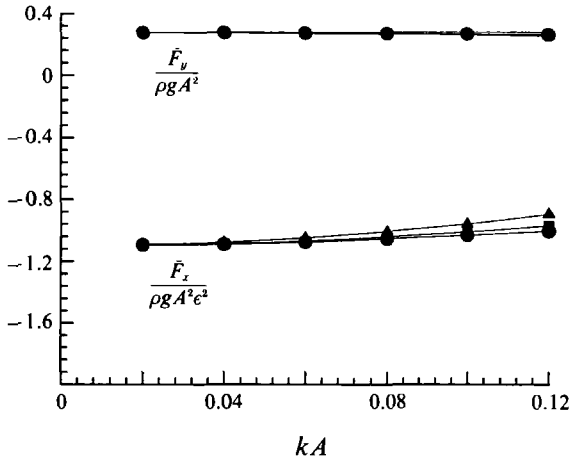

FIGURE 8. Dependence of the horizontal and vertical drift forces on the incident wave slope $\epsilon = kA$. $M = 2$ (▲), $M = 3$ (■), and $M = 4$ (●). ($kR = 0.4$, $H/R = 2$.)

0.4 and $kH = 0.8$). Figure 8 shows the numerical results ($M = 2, 3, 4$) for $\bar{F}_x$ and $\bar{F}_y$ which have been normalized by their expected leading-order magnitudes proportional to ϵ^4 and ϵ^2 respectively. As expected, these normalized values approach constant asymptotes for small kA. For the mean uplift force, this asymptote is well predicted by the second-order value based on the (analytic) first-order potential only. Hereafter, we concentrate on the 'truly' nonlinear horizontal drift force.

To assist us in understanding the horizontal drift force results, it is useful to obtain an estimate based on the conservation of energy and linear horizontal momentum. We neglect wave reflection (cf. §4.2) and consider the incident/transmitted wave amplitudes far up/down stream of the body. Let a_n and b_n be the nth harmonics of the incident and transmitted wave amplitudes respectively. Following Longuet-Higgins (1977), we further assume that all $a_n, b_n, n = 1, 2, \ldots$ are of the same order of magnitude and consider only 'bi-linear' interactions. With this assumption, application of the conservation of horizontal momentum yields an expression for the horizontal drift force which, to leading order, is given by

$$\bar{F}_x = \frac{\rho g}{4} \sum_{n=1} (a_n^2 - b_n^2). \tag{29}$$

From the conservation of energy, a_n and b_n are related by

$$\sum_{n=1} a_n^2/n = \sum_{n=1} b_n^2/n. \tag{30}$$

For Stokes incident waves, the first-harmonic amplitude a_1 is much greater than all other harmonics, so that we can neglect all $a_n, n > 1$ terms in (29) and (30). Substituting (30) into (29), we obtain finally

$$\bar{F}_x = -\frac{\rho g}{4} \sum_{n=2} b_n^2 (n-1)/n. \tag{31}$$

Equation (31) provides a way to estimate $\bar{F}_x$ given the transmitted wave harmonic amplitudes, and is a generalization of a result of Longuet-Higgins (1977) who included the first (b_2) term only. Note that in view of the 'bi-linear' assumption,

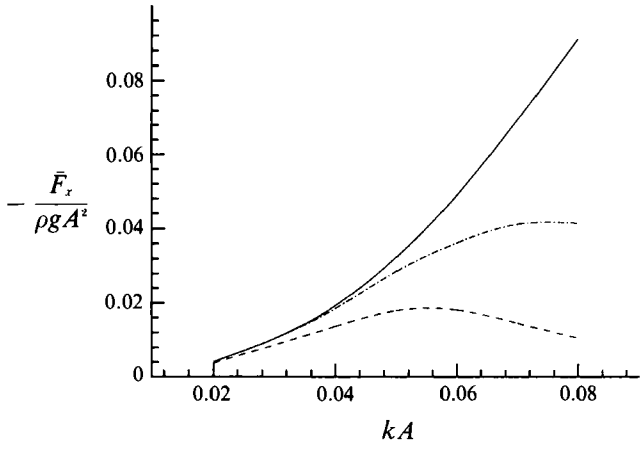

FIGURE 9. Comparison of the horizontal drift force as a function of wave slope kA. The results are from direct high-order simulation with $M = 4$ (——); equation (31) using b_2 only (– – –); and equation (31) including b_2 and b_3 (—·—). ($kR = 0.4$, $H/R = 1.5$.)

higher-order interaction terms involving different harmonics (especially in the transmitted waves) are neglected in (29) and (30). Therefore (31) must be considered only as an approximate formula valid primarily for small wave steepness.

The prediction using (31) based on computed transmitted wave amplitudes is compared to that obtained by direct pressure integration in figure 9, where $\bar{F}_x$ is plotted as a function of kA. For small wave slopes, $kA < \sim 0.03$, (31) with only b_2 provides an adequate estimate. As kA increases further beyond ~ 0.05, b_2 reaches its maximum (cf. figure 3) and consequently so does the estimated drift force based on b_2, while the actual $\bar{F}_x$ continues to increase. The prediction based on (31) is improved if third-harmonic transmitted waves are taken into account, and the discrepancy is not appreciable until after $kA \sim 0.05$. Not completely unexpectedly, applications of (31) with even higher transmitted wave harmonics included (not shown) do not produce appreciable further improvements unless wave reflection and higher-order interactions are also considered. In so far as independent ways are used to obtain $\bar{F}_x$, figure 9 can be considered a further validation of our predictions of the fourth-order negative drift force.

In the context of a frequency-domain perturbation approach, we see from the expression for the pressure on the cylinder (14) that steady forces must be due to quadratic interactions of the perturbation potentials $\tilde{\phi}_n^{(m)}$. Specifically, the horizontal drift force on the circular cylinder is given, up to fourth order in the wave slope, by

$$\bar{F}_x \sim \int_0^{2\pi} \mathrm{d}\theta\, R\cos\theta(\nabla\tilde{\phi}_1^{(1)}\cdot\nabla\tilde{\phi}_1^{(1)*} + 2\nabla\tilde{\phi}_1^{(1)}\cdot\nabla\tilde{\phi}_1^{(3)*} + \nabla\tilde{\phi}_2^{(2)}\cdot\nabla\tilde{\phi}_2^{(2)*} + \nabla\tilde{\phi}_0^{(2)}\cdot\nabla\tilde{\phi}_0^{(2)*} + \text{c.c.}), \quad (32)$$

where * denotes complex conjugate, and c.c. the complex conjugate of the preceding terms. Equation (32) is obtained by direct integration of the pressure over the cylinder and taking the time average.

As shown by Ogilvie (1963), the first term in (32), which is second order, makes no contribution to the mean force, so that the drift force results from the remaining three fourth-order terms. For later convenience, we denote the second, third and fourth terms in (32) by $\bar{F}_{11}$, $\bar{F}_{22}$, and $\bar{F}_{00}$ respectively. With the present accurate high-

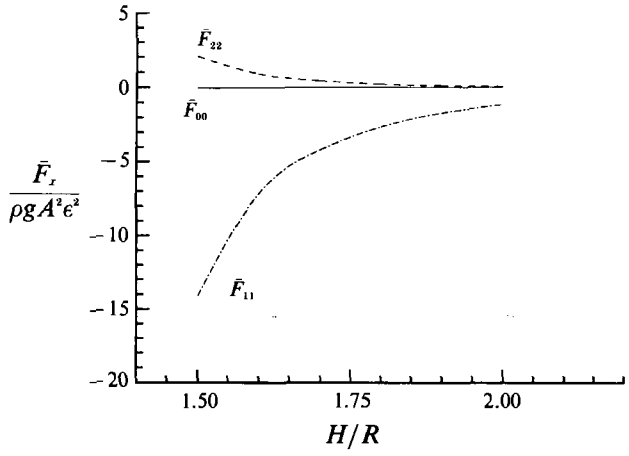

FIGURE 10. Contributions of the three fourth-order components $\bar{F}_{00}$, $\bar{F}_{11}$, $\bar{F}_{22}$ to the mean horizontal drift force as a function of submergence H/R. ($kR = 0.4$, $\epsilon = kA = 0.04$.)

order (albeit time-domain) results, it is possible to deduce the respective contributions of $\bar{F}_{11}$, $\bar{F}_{22}$, and $\bar{F}_{00}$ to $\bar{F}_x$. (We solve the problem up to $M = 3$, obtain the steady-state potential $\Phi^{\langle 3\rangle}$, from which we determine the amplitudes $\phi_0^{\langle 3\rangle}$, $\phi_1^{\langle 3\rangle}$, and $\phi_2^{\langle 3\rangle}$ via harmonic analysis. Using (26), we calculate $\bar{F}_{22}$ and $\bar{F}_{00}$ to leading (fourth) order using $\phi_2^{\langle 3\rangle}$ and $\phi_0^{\langle 3\rangle}$ instead of $\tilde{\phi}_2^{(2)}$ and $\tilde{\phi}_0^{(2)}$. Finally, since there is no drift force due to $\tilde{\phi}_1^{(1)}$ (and there is no $\tilde{\phi}_1^{(2)}$), we deduce that $\bar{F}_{11}$ is produced by the self-interaction of $\phi_1^{\langle 3\rangle}$.)

The drift force components $\bar{F}_{11}$, $\bar{F}_{22}$, and $\bar{F}_{00}$ are plotted in figure 10 as functions of H/R. As expected, all three components have magnitudes that diminish with body submergence. Overall, the magnitude of $\bar{F}_{00}$ is much smaller than $\bar{F}_{11}$ and $\bar{F}_{22}$, which implies that the self-interaction of zeroth-harmonic waves has negligible effect on $\bar{F}_x$. More importantly, we note that for any body submergence, $\bar{F}_{22}$ is non-negative, while $\bar{F}_{11}$ is always negative and much greater in magnitude. Thus, the negative horizontal drift force is a result of the difference between these two magnitudes. An immediate consequence of this is that one indeed needs to solve the third-order perturbation problem to obtain $\bar{F}_x$, and a frequency-domain solution up to and including $\tilde{\phi}^{(2)}$, for example, is inadequate, and in fact would produce the wrong sign for the horizontal drift force!

One advantage of having identified the components in (32) is that one can now deduce how $\bar{F}_x$ would, in principle, attenuate with body submergence. Specifically, for small kR, we expect the self-interaction of first-harmonic waves to decay as $\bar{F}_{11} \sim \mathrm{e}^{-2kH}$, and that for second-harmonic waves as $\bar{F}_{22} \sim \mathrm{e}^{-8kH}$. These are qualitatively confirmed in figure 10 (although the actual attenuation rates are somewhat slower, probably due to the effect of finite body radius). By accounting for these submergence dependencies (and magnitudes) of $\bar{F}_{11}$ and $\bar{F}_{22}$, it is evident that in general $\bar{F}_x$ is negative and dominated by $\bar{F}_{11}$ except possibly for small submergence. As kH decreases, $\bar{F}_{22}$ increases more rapidly than $\bar{F}_{11}$, so that at very shallow submergence, the magnitude of the negative drift force may be reduced appreciably by $\bar{F}_{22}$. This is in qualitative agreement with the experimental observations of Miyata *et al.* (1988) and Inoue & Kyozuka (1984).

Finally, we point out that by considering the radiation stress (Longuet-Higgins 1977), the horizontal drift force is related to the mean set-down above the cylinder. Figure 11 plots the separate contributions to the mean set-down associated with $\bar{F}_{22}$

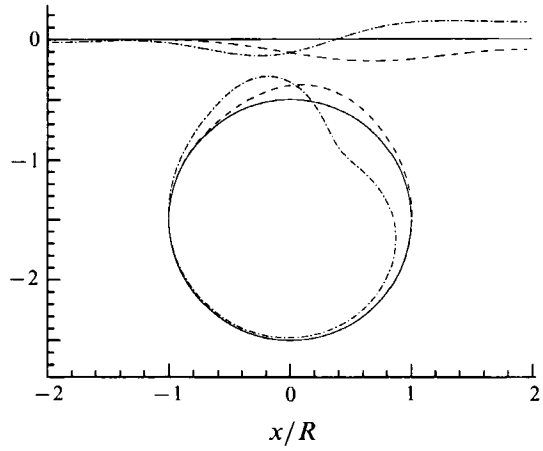

FIGURE 11. Separate contributions associated with the self-interactions of the first-harmonic $(\,)_{11}$ and second-harmonic $(\,)_{22}$ waves to the mean free surface: $\bar{\eta}_{11}/kA^2$ (—·—); $\bar{\eta}_{22}/kA^2$ (– – –); and the mean pressure on the cylinder surface: $5\bar{p}_{11}/\rho gkA^2$ (—·—); $5\bar{p}_{22}/\rho gkA^2$ (– – –). Pressure is plotted positive into the body. ($kR = 0.4$, $H/R = 1.5$, $kA = 0.04$.)

and $\bar{F}_{11}$. The corresponding time-averaged pressure distributions on the cylinder associated with these two interactions are also shown. The larger (smaller) downstream mean set-down for $\bar{F}_{22}$ ($\bar{F}_{11}$) and the distribution of the mean pressure provide immediate qualitative confirmation of the positive (negative) sign and magnitude of its contribution to $\bar{F}_x$. (Note that this is not inconsistent with figure 9 since b_1 depends on $\tilde{\phi}_1^{(3)}$.)

When the body submergence is sufficiently small and/or the incident wave steepness is sufficiently large, wave breaking above the cylinder must be expected and the present method and results are no longer applicable. It has been suggested (Longuet-Higgins 1977) that wave breaking provides the dominant contribution to the negative drift force. This is not completely supported by measurements (for example, Miyata *et al.* 1988), which indicate that as the body submergence is reduced and wave breaking therefore enhanced, the magnitude of the negative drift force may, in fact, decrease. Although the present method is not valid for breaking (and near-breaking) waves, our results compare well with experimental data (not in the breaking range) and explain the potential flow mechanism for the negative drift force. Not insignificantly, we are also able to offer an explanation for the observed decrease of its magnitude with small submergence (due to $\bar{F}_{22}$) which may occur even in the presence of intensifying wave breaking.

5. Conclusions

An arbitrary high-order spectral method has been developed to study the nonlinear interactions of waves with a submerged body. By using global spectral representations for the body and free-surface singularity distributions, exponential convergence with the numbers of body and free-surface modes and with perturbation order M is achieved. With the use of fast transform techniques, the computational burden remains effectively a linear function of the number of unknown modes and of M.

To illustrate the efficacy of this method, we perform a detailed study of the nonlinear wave diffraction by a submerged circular cylinder. Extensive convergence

tests are carried out to validate the accuracy and its dependence on the computational parameters. Results are presented for the harmonic amplitudes of the transmitted and reflected waves, and the mean and harmonic amplitudes of the forces on the cylinder. Corroborations with theoretical and computational predictions and experimental measurements are made whenever they are available. The comparisons are in uniformly good agreement. Of special interest is our quantification of the horizontal drift force which is fourth order in the incident wave steepness and negative, and is shown to be primarily a result of the interaction between the first- and third-order first-harmonic waves.

We remark that the present method can be immediately generalized to three dimensions and to problems with forward speed. In the former case, the expansions (8) are simply replaced by a double-Fourier series for the free surface, and a Fourier–Chebyshev expansion, say, for the submerged body:

$$\sigma^{(m)}(\varphi,\theta,t)=\sum_j\sum_l \sigma_{jl}^{(m)}(t)\,\mathrm{e}^{\mathrm{i}j\varphi}T_l(1-2\theta/\pi), \tag{33}$$

where φ,θ are respectively the polar and azimuthal angles of a point on the body surface with respect to its centre.

This research is financially supported by the Office of Naval Research and the National Science Foundation. Some computations were performed on a Cray Y-MP at the Pittsburgh Supercomputer Center, and on a Cray-2S at Cray Research, Inc.

REFERENCES

BENNEY, D. J. 1962 Nonlinear gravity wave interactions. *J. Fluid Mech.* **14**, 577–589.

CHAPLIN, J. R. 1984 Nonlinear forces on a horizontal cylinder beneath waves. *J. Fluid Mech.* **147**, 449–464.

COINTE, R. 1989 Nonlinear simulation of transient free surface flows. In *Proc. 5th Intl Conf. Num. Ship Hydro., Hiroshima*, pp. 239–250. Washington: National Academy Press.

CRAWFORD, D. R., LAKE, B. M., SAFFMAN, P. G. & YUEN, H. C. 1981 Stability of weakly nonlinear deep-water waves in two and three dimensions. *J. Fluid Mech.* **105**, 177–191.

DEAN, W. R. 1948 On the reflection of surface waves by a submerged circular cylinder. *Proc. Camb. Phil. Soc.* **44**, 483–491.

DOMMERMUTH, D. G., LIN, W. M., YUE, D. K. P., RAPP, R. J., CHAN, E. S. & MELVILLE, W. K. 1988 Deep water plunging breakers: a comparison between potential theory and experiments. *J. Fluid Mech.* **189**, 423–442.

DOMMERMUTH, D. G. & YUE, D. K. P. 1987*a* A high-order spectral method for the study of nonlinear gravity waves. *J. Fluid Mech.* **184**, 267–288 (referred to herein as DY).

DOMMERMUTH, D. G. & YUE, D. K. P. 1987*b* Nonlinear three-dimensional wave–wave interactions using a high-order spectral method. In *Symp. on Nonlinear Wave Interactions in Fluids*, Boston, USA.

FORNBERG, B. & WHITHAM, G. B. 1978 A numerical and theoretical study of certain nonlinear wave phenomena. *Phil. Trans. R. Soc. Lond.* A **289**, 373–404.

FRIIS, A. 1990 A second order diffraction forces on a submerged body by a second order Green function method. *Fifth Intl Workshop on Water Waves and Floating Bodies*, Manchester, UK, 73–74.

GRUE, J. 1991 Nonlinear water waves at a submerged obstacle or bottom topography. Preprint Series of Institute of Mathematics, University of Oslo. No. 2, 1–21.

INOUE, R. & KYOZUKA, Y. 1984 On the nonlinear wave forces acting on submerged cylinders. *J. Soc. Nav. Arch. Japan* **156**, 115–127.

LONGUET-HIGGINS, M. S. 1977 The mean forces exerted by waves on floating or submerged bodies with applications to sand bars and wave power machines. *Proc. R. Soc. Lond.* A **352**, 463–480.

LONGUET-HIGGINS, M. S. & COKELET, E. D. 1976 The deformation of steep surface waves on water. I a numerical method of computation. *Proc. R. Soc. Lond.* A **350**, 1–26.

MCIVER, M. & MCIVER, P. 1990 Second-order wave diffraction by a submerged circular cylinder. *J. Fluid Mech.* **219**, 519–529.

MIYATA, H., KHALIL, G., LEE, Y.-G. & KANAI, M. 1988 An experimental study of the nonlinear forces on horizontal cylinders. *J. Kansai Soc. N.A. Japan* **209**, 11–23.

OGILVIE, T. F. 1963 First- and second-order forces on a cylinder submerged under a free surface. *J. Fluid Mech.* **16**, 451–472.

ORSZAG, S. A. 1971 Numerical simulation of incompressible flows within simple boundaries: accuracy. *J. Fluid Mech.* **49**, 75–112.

PALM, E. 1991 Nonlinear wave reflection from a submerged circular cylinder. *J. Fluid Mech.* **233**, 49–63.

PHILLIPS, O. M. 1960 On the dynamics of unsteady gravity waves of finite amplitude. Part 1. The elementary interactions. *J. Fluid Mech.* **9**, 193–217.

SALTER, S. H., JEFFREY, D. C. & TAYLOR, J. R. M. 1976 The architecture of nodding duck wave power generators. *The Naval Arch.* 21–24.

SCHWARTZ, L. W. 1974 Computer extension and analytic continuation of Stokes' expansion for gravity waves. *J. Fluid Mech.* **62**, 553–578.

STANSBY, P. K. & SLAOUTI, A. 1983 On non-linear wave interaction with cylindrical bodies: a vortex sheet approach. *Appl. Ocean Res.* **6**, 108–115.

URSELL, F. 1950 Surface waves on deep water in the presence of a submerged circular cylinder I. *Proc. Camb. Phil. Soc.* **46**, 141–152.

VADA, T. 1987 A numerical solution of the second-order wave-diffraction problem for a submerged cylinder of arbitrary shape. *J. Fluid Mech.* **174**, 23–37.

VINJE, T. & BREVIG, P. 1981 Numerical calculations of forces from breaking waves. *Intl Symp. Hydro. Ocean Engng, Norway.*

WU, G. X. 1991 On the second order wave reflection and transmission by a horizontal cylinder. *Appl. Ocean Res.* **13**, 58–62.

ZAKHAROV, V. E. 1968 Stability of periodic waves of finite amplitude on the surface of a deep fluid. *J. Appl. Mech. Tech. Phys.* **9**, 190–194 (English transl.).

ZAROODNY, S. J. & GREENBERG, M. D. 1973 On a vortex sheet approach to the numerical calculation of water waves. *J. Comput. Phys.* **11**, 440–446.